

System identification and a linear time invariant-model of an insect-sized flapping-wing micro air vehicle

Benjamin M. Finio, Néstor O. Pérez-Arancibia, and Robert J. Wood

Abstract—Flapping-wing robots typically include numerous nonlinear elements, such as nonlinear geometric and aerodynamic components. For an insect-sized flapping-wing micro air vehicle (FWMAV), we show that a linearized model is sufficient to predict system behavior with reasonable accuracy over a large operating range, not just locally around the linearization state. The theoretical model is verified against an identified model from a prototype robotic fly and implications for vehicle design are discussed.

I. INTRODUCTION

Research in the areas of insect flight and biologically-inspired flapping-wing micro air vehicles (FWMAVs) has expanded significantly in the last decade, motivated by the need for small-scale, agile aircraft that can maneuver in confined or dangerous spaces. Dynamic modeling of such FWMAVs typically includes several nonlinear elements, such as mechanism kinematics of linkages that are used to connect motors or other actuators to flapping wings [1], nonlinear aerodynamic forces [2], or nonlinear actuator effects such as saturation and hysteresis [3]. Wings typically flap through large angular ranges while also undergoing large changes in angle of attack, so some standard methods for linearizing dynamic models may not be appropriate. For example, the small angle assumption ($\sin \theta \approx \theta$) is usually only considered valid over a range of $\pm 15^\circ$, whereas wings may flap through a stroke amplitude as great as 120° in some FWMAVs [4] and approach 180° in some insects [5]. Lift and drag coefficients from a quasi-steady aerodynamic model typically used to predict aerodynamic forces on flapping wings [6] are functions of angle of attack and thus can vary greatly throughout a single stroke as the angle of attack changes [7]. As a result, complete dynamic models of FWMAV systems are usually highly nonlinear and time varying.

Numerous studies have investigated nonlinear modeling of FWMAVs, frequently with attention to design and optimization of elastic elements which allow a flapping system to be driven at resonance, thus reducing or eliminating the inertial cost associated with accelerating and decelerating the wing [8], [9], [10], [11], [12]. However, such studies typically focus on the addition of a spring element to an existing MAV system, without consideration for redesigning actuators, linkages or wings. Other studies, such as [13], have taken a more integrated approach to vehicle design, including wing, actuator and transmission elements, accounting for full nonlinear dynamics. Each component can have an important

The authors are with the School of Engineering and Applied Sciences and the Wyss Institute for Biologically Inspired Engineering, Harvard University, Cambridge, MA 02138. bfinio@fas.harvard.edu, nperez@seas.harvard.edu, rjwood@eecs.harvard.edu.

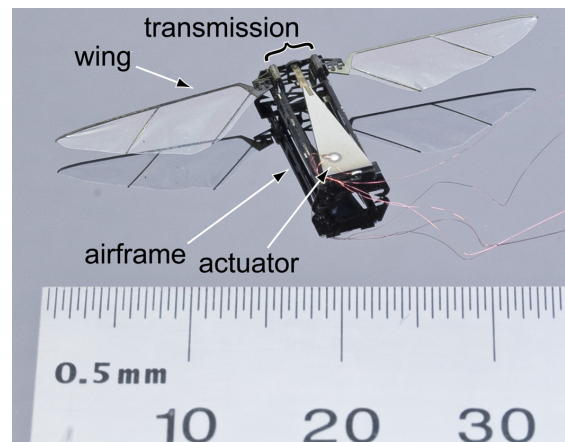


Fig. 1. A recent prototype of the Harvard Microrobotic Fly, an insect-sized flapping-wing micro air vehicle.

effect on overall system dynamics and thus vehicle performance - for example, changing the wing shape will affect both its inertial properties and aerodynamic damping forces, whereas changing a linkage system or gearbox will affect how torques map from the motor frame of reference to the wing.

Here, we seek to show that a *linear* model can serve as a simple, useful design tool to predict resonant behavior of a system driven by a harmonic actuator, and examine the validity of a linearized model in the presence of various nonlinearities mentioned above. Such a model should accurately account for changes to system parameters such as wing shape, actuator size and transmission geometry in order to examine their effects on resonant behavior. Accurately predicting resonant behavior will allow the design of a system with maximum power transfer from actuators to the load (in this case, the air) or an optimal lift/weight ratio.

An alternative approach to developing a physics-based, ground-up nonlinear model and then linearizing it is to use system identification. Here, a linear model can be derived by experimentally measuring a system's response to chosen inputs and estimated disturbances. This is commonly used, for example, to characterize the dynamics of hovering rotary-wing MAVs moving in three-dimensional space, due to the difficulty of calculating parameters such as body inertia and drag terms for a vehicle with complex shape [14]. We define such a problem as modeling the “external” dynamics of the system. The MAV itself is treated as a black box, and system inputs are mapped to motions in three dimensional space; interior interactions of power supplies, actuators, linkages

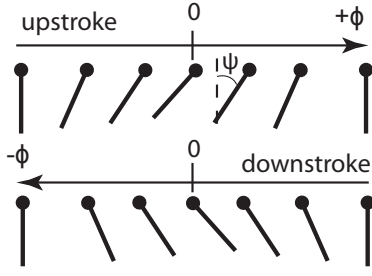


Fig. 2. View of a wing chord section during flapping. As the wing flaps (ϕ), it rotates passively about a spanwise axis (ψ). Thus lift is generated on both the upstroke and downstroke.

and airfoils are not modeled separately. Such experiments are useful for designing a flight controllers for a predetermined vehicle design. However, for the purposes of vehicle design itself, we must characterize the “internal” dynamics - for example, the relationship between an electrical control signal and actuator motion, or wing movement and resulting aerodynamic forces.

The Harvard Microrobotic Fly (HMF) is an approximately 60mg, 3cm-wingspan FWMAV inspired by Dipteran insects (Fig. 1). It consists of four main components, each analogous to a biological counterpart: the airframe (exoskeleton), actuator (flight muscles), transmission (thorax), and airfoils (wings). The actuator, a piezoelectric cantilever beam, provides an oscillatory mechanical input to a symmetric fourbar transmission, which converts linear motion of the tip of the actuator to flapping motion of the wings. Each wing rests on a hinge that acts as a torsional spring, allowing the wing to rotate passively due to aerodynamic and inertial forces as it is flapped. Thus the wing can generate lift on both the upstroke and the downstroke (Fig. 2). Using a simple lumped parameter model, [1] predicted an undamped natural frequency of 170 Hz, with measured resonance of 110 Hz in the experimental prototype. In this paper, we seek to improve on this analysis and present a linearized model that can accurately predict the frequency domain response of an actuator-transmission-wing system and compare this theoretical model to a linear model derived from experimental data using system identification.

The rest of the paper is organized as follows. In Section II the experimental setup and development of the identified model are described briefly. Section III presents the development of a linearized dynamic model. Section IV compares the frequency-domain responses of the identified and theoretical models using Bode diagrams. Section V discusses implications of the results on vehicle design and usefulness of the theoretical model as a design tool, particularly how physical parameters of the system affect the resonant response. Further considerations and future work are discussed in Section VI.

II. EXPERIMENTS

We use the experimental setup in Fig. 3, which is a modified version of the one in [2], a single wing version of robotic flapper presented in [1] designed for aerodynamic testing. This setup allows simultaneous measurement of the

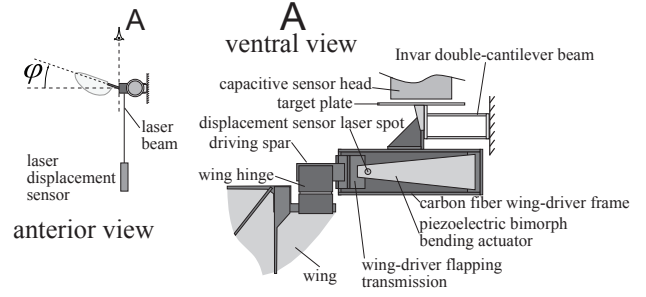


Fig. 3. Diagram of the experimental setup for measuring lift forces and displacement of the actuator tip. The wing-driver is attached to an Invar double cantilever beam, whose deflection is measured by a capacitive displacement sensor. This deflection is proportional to the lift force. The displacement of the actuator tip is measured using a CCD laser displacement sensor.

displacement of the tip of the piezoelectric actuator as well as measurement of the instantaneous lift force (which is not purely aerodynamic since it will include an inertial component due to wing rotation). As shown in Fig. 3, the wing driver mechanism is mounted on the end of a double-cantilever beam, whose deflection is measured with a capacitive displacement sensor (CDS). For small beam deflections, there is a linear relationship between deflection and lift force. Further details on the design, fabrication and calibration of the CDS-based force sensor are given in [2] and [15]. The other variable measured is the displacement of the actuator tip. As shown in Fig. 3, this is done using a noncontact charge-coupled device (CCD) laser displacement sensor (Keyence LK-031), which is located close to the actuator tip. The sensor laser reflection on the actuator is depicted as a circular spot in Fig. 3.

A discrete-time state-space representation of the system is found using a subspace algorithm as in [16]. The input to the system is an electrical signal from a D/A board which is amplified through a high-voltage amplifier and sent to the actuator, and the output is an analog voltage from the CCD sensor used to measure deflection of the actuator tip, which is then sampled and recorded with an A/D board. We refer to the actual continuous-time system as P and the discrete-time identified model as P_I . A block diagram of this system is shown in Fig. 4. Fig. 5 shows Bode plots of the identified 48th-order linear model and a reduced 4th-order model. The magnitude response has been normalized to have 0 dB gain at DC. Note that P_I has two prominent resonant peaks, around 127 Hz and 750 Hz respectively. Understanding the 120 Hz peak is of particular interest since this falls within the typical range of operation of the robot.

The higher-frequency dynamics may arise due to a variety of causes, such as higher-order dynamic components within the system, such as vibration of the wing itself or an unknown aerodynamic effect; or vibration of components that are considered mechanical ground, and thus perfectly rigid, in the model, such as the airframe or lift sensor (note that the lift sensor itself has a resonant frequency of approximately 1kHz). At this point, any discussion of the root causes of these higher order dynamics is purely speculative, and thus

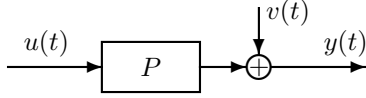


Fig. 4. A block diagram of the experimental system. The actual open-loop plant P is driven by input voltage signal to the actuator $u(t)$. The measured output $y(t)$ is the displacement of the actuator tip, which will include effects from all aggregated output disturbances $v(t)$ acting on the system (such as aerodynamic forces).

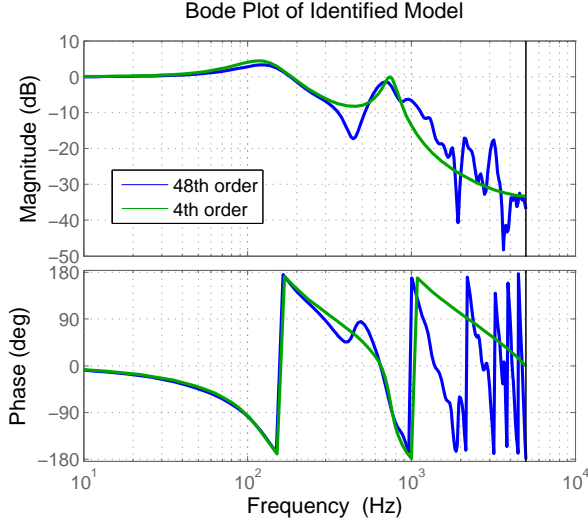


Fig. 5. Bode plot of the identified discrete-time model P_I of the system depicted in Fig. 4. The input to the system is the voltage sent through an amplifier to the actuator, and measured output is the voltage of the CCD sensor which corresponds to actuator displacement.

not investigated further in this paper. Regardless of their source, feedback control of the piezoelectric actuator position can be used to cancel out undesired vibrational modes [16].

III. DEVELOPMENT OF LINEAR MODEL

The identified model P_I gives us an empirical reference with which we can evaluate the quality of a linear, lumped-parameter model. There are three primary mechanical components of interest in formulating the dynamic model: the actuator, transmission, and wings. The three components are connected and each has associated nonlinear geometric, inertial, damping or elastic behavior (Fig. 6). Since the system only has one mechanical degree of freedom, it can be simplified to the one illustrated in Fig. 7. We assume the fourth component, the airframe, acts as a rigid mechanical ground and thus has no relevant dynamic properties. Here, we treat the linearization of each component individually, then synthesize these components to develop the full linear model.

A. Actuator

Piezoelectric actuators can be subject to numerous nonlinear effects, including creep, saturation, hysteresis, and electric field-dependent stiffness (and thus resonant frequency). See [3] for a detailed analysis of these effects. For modeling

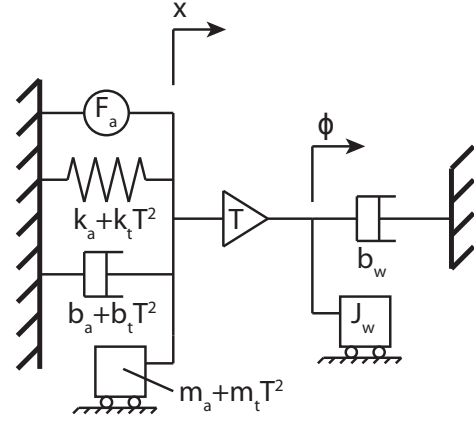


Fig. 6. A lumped-parameter representation of the dynamic system to be modeled. The subscripts a , t and w stand for actuator, transmission and wing respectively. The system consists of an actuator connected to the wings by a mechanical transmission. Each component has its own geometric, inertial, damping and elastic terms, many of which are nonlinear but can be approximated by linear models. The transmission itself can have dynamic properties, which are mapped back to the actuator frame x via the transmission ratio T . It is important to note that x and ϕ are kinematically related through the transmission T , so the system pictured only has one degree of freedom, and therefore can be reduced to the equivalent diagram shown in Fig. 7.

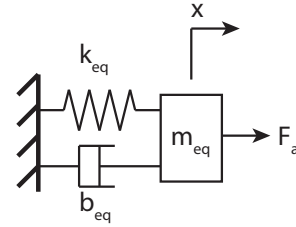


Fig. 7. The elements in Fig. 6 can be lumped into equivalent stiffness, damping and inertial parameters (still nonlinear) in a single coordinate frame, either x or ϕ .

purposes, a piezoelectric actuator can be treated as a two-port element that transduces voltage and current to force and velocity. See [17] for more details on dynamic modeling of the actuator.

Three key assumptions allow treatment of the actuator as a linear element. First, the actuator is driven by an ideal voltage source, therefore a voltage-driven piezoelectric actuator is equivalent to a force source in the mechanical domain. Second, the resonant frequency of the actuator (~ 1000 Hz) is much higher than the typical operating frequencies of interest for the FWMAV in question (~ 100 Hz), thus we can assume quasi-static operation of the actuator. This is expected based on several previous studies of piezoelectric actuators which have recorded the frequency-domain magnitude response of the actuator tip displacement for clamped-free boundary conditions [18], [19]. We measure the *force* response of an actuator to a voltage input, including phase information, under clamped-clamped and clamped-pin/roller boundary conditions; this is due to the difficulty of measuring force under clamped-free boundary conditions, which requires construction of a dynamometer as in [20]. The

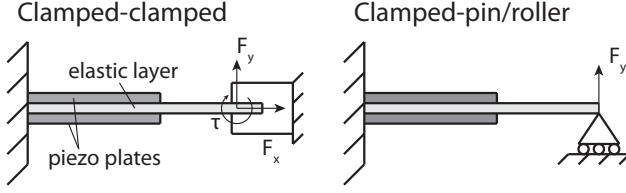


Fig. 8. A side view of the experimental setup used to measure actuator voltage-force response. Force output of the actuator is measured under clamped-clamped and clamped-pin/roller conditions using a six-axis force/torque sensor (ATI Nano 17). The latter case allows measurement of pure vertical force at the tip, while clamped-clamped conditions measure both horizontal and vertical forces and a moment. The clamped-pin/roller condition better approximates the operating conditions when the actuator is attached to a transmission-wing system.

resonant frequency of a beam, if measured under one set of boundary conditions, can be adjusted for different boundary conditions via a scaling factor (see [21], p 3-73), thus we can approximate the resonant frequency of a clamped-free actuator using these tests.

A diagram of the experimental setup is shown in Fig. 8. Force data is recorded with a six-axis force/torque sensor (ATI Nano 17), and a linear model is derived using the same system identification techniques used to create a model of the robotic wing flapper (Fig. 9). The identified model shows that, at low frequencies, the force output has a flat-band response (i.e. constant gain and zero phase difference) for both sets of boundary conditions, suggesting that that force is simply proportional to voltage at low frequencies. The dynamics at higher frequencies may arise due to resonance of the clamping mechanism used to hold the actuator in place, sensor noise, or other factors; but for a worst-case scenario, we can assume an actuator resonance of just over 1 kHz. Based on the scaling factors in [21], a clamped-hinged beam will be four times stiffer than a clamped-free beam, thus we would still expect a *minimum* actuator resonance of 250 Hz, outside the range of interest for our MAV. In practice, the resonant frequency of the actuators is expected to be much higher.

Lastly, the frequency and field-dependent, thus nonlinear, actuator damping is not a significant source of loss [22], therefore can be neglected relative to the aerodynamic damping. From the static analysis of the actuators in question in [19], we expect the force exerted by an actuator to simply be proportional to the applied voltage. Thus for sinusoidal voltage excitation, the force applied by the actuator to the mechanical system is simply

$$F_a = F_b \sin(2\pi ft) \quad (1)$$

where F_b is the maximum (blocked) force of the actuator, a function of actuator geometry, material properties and applied voltage as calculated in [19], and f is the drive frequency. Neglecting nonlinear softening effects, the elastic deformation of the actuator acts as a linear mechanical spring with spring constant k_a , also available based on the derivation in [19]. As mentioned above, we neglect the actuator damping term b_a in Fig. 6.

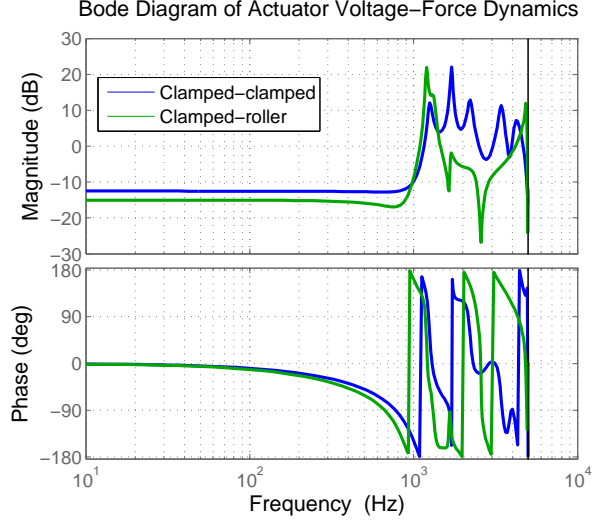


Fig. 9. The identified model of a cantilever piezoelectric actuator shows that in the frequency range of interest for the FWMAV, the force output of the actuator is flat and in phase with the voltage input. This suggests that it is reasonable to treat the force as simply proportional to the applied voltage. High-frequency dynamics are ignored as they may arise from resonance of the clamp, sensor noise or other sources that are mistaken by the system identification model as dynamic behavior, and the frequency range over 1 kHz is not of interest for the FWMAV in question.

B. Transmission

The transmission consists of two symmetric slider-crank fourbar mechanisms (or, for the single-wing driver used in these experiments, only a single fourbar). Their input links are rigidly connected so the entire transmission is only 1DOF. Half of the transmission is shown in Fig. 10. The transmission physically consists of stiff carbon fiber links connected by flexible polymer joints - a *pseudo-rigid body* assumption models the carbon fiber links as rigid and the flexures as ideal revolute joints with torsional springs [23]. This allows kinematic analysis of the transmission to map actuator input x to wing flapping angle ϕ using the dimensions defined in Fig. 10. $\phi(x)$ is given by

$$\phi = \cos^{-1} \left(\frac{(L_y - x)^2 + C_1}{C_2 \sqrt{L_3^2 + (L_y - x)^2}} \right) + \tan^{-1} \left(\frac{L_3}{L_y - x} \right) + \tan^{-1} \left(\frac{L_2 - L_4}{L_3} \right) - \frac{\pi}{2} \quad (2)$$

where

$$L_y = L_1 + L_2 - L_4 \quad (3)$$

$$C_1 = L_3^2 + (L_2 - L_4)^2 - L_1^2 + L_3^2 \quad (4)$$

$$C_2 = 2\sqrt{L_3^2 + (L_2 - L_4)^2}. \quad (5)$$

For small displacements, (2) can be simplified greatly, and the transmission simply acts as a lever, i.e.,

$$\phi = Tx \quad (6)$$

where $T = 1/L_3$. For the single-wing flapping device used in these experiments, the transmission dimensions are

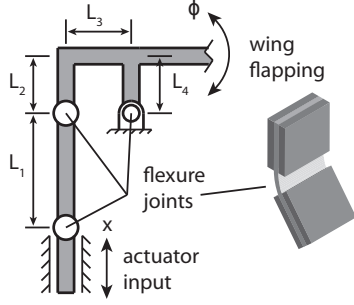


Fig. 10. One-half of the fourbar transmission is pictured. The transmission kinematically relates actuator displacement x to wing flapping angle ϕ . Flexure joints (inset) act as revolute joints with attached torsional springs.

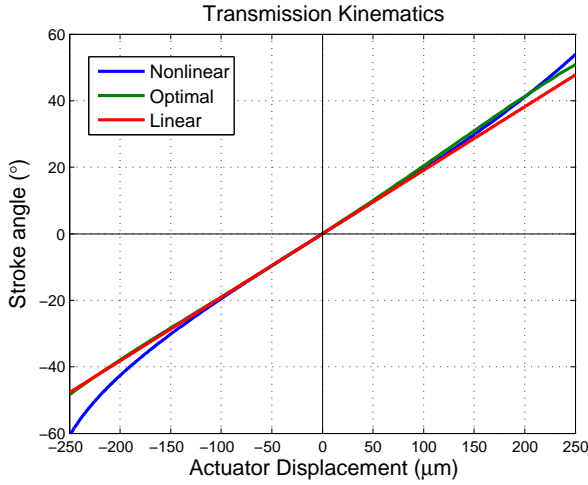


Fig. 11. The nonlinear and linear transmission kinematics plotted over actuator position ranging across $\pm 250 \mu\text{m}$. The linearization is quite accurate for wing motions up to $\pm 20^\circ$ and begins to deviate from the nonlinear kinematics as wing angles approach $\pm 60^\circ$. Transmission geometry can be optimized to improve the linearity of the response.

$L_1 = 300 \mu\text{m}$, $L_2 = 500 \mu\text{m}$, $L_3 = 300 \mu\text{m}$, and $L_4 = 630 \mu\text{m}$. The nonlinear and linearized kinematics for this geometry are plotted in Fig. 11. As expected, the small angle assumption is valid in the range of roughly $\pm 20^\circ$, however the actual stroke angle begins to deviate from the linearized angle for larger actuator displacements. It is possible to optimize transmission linearity numerically by defining a cost function such as the square of the difference between the derivative $d\phi/dx$ and the ideal linear transmission ratio T , and minimizing this function using the “fmincon” algorithm in Matlab. The kinematics for an optimal geometry with link lengths $L_1 = 312 \mu\text{m}$, $L_2 = 400 \mu\text{m}$, $L_3 = 291 \mu\text{m}$, and $L_4 = 498 \mu\text{m}$ are shown in Fig. 11 as well.

The elastic deformation of the flexures stores potential energy and thus must be included in a dynamic model. While this element will be nonlinear due to the nonlinear kinematics, linearization of the kinematics means the flexures can be treated as torsional springs with spring constant k_t . Damping and inertia of the transmission flexures and linkages are neglected, as these values are quite small relative to the aerodynamic damping and inertia of the wings [24].

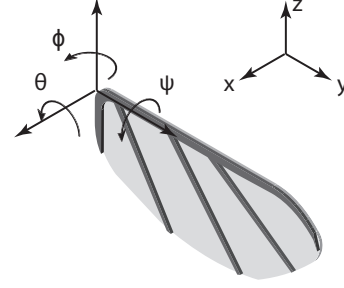


Fig. 12. The global xyz coordinate system is fixed to the vehicle airframe. The wing flaps about the ϕ axis, which remains parallel with the global z axis. The ψ and θ axes rotate with the leading edge of the wing. In addition to flapping about the ϕ axis, the wing also rotates about the ψ axis. Deviations from a flat stroke plane (θ) are not addressed here.

C. Wings

1) *Inertia*: As discussed earlier, the wing flaps about one axis while rotating about its longitudinal axis (see Fig. 12). Coupling between these degrees of freedom leads to nonlinear terms in the equations of motion (for brevity the derivation is not reproduced here, see [2] for details). Analysis can be greatly simplified if the wing is treated as a rod rotating about a single axis ϕ , and the second axis of rotation ψ is ignored. This may be a reasonable assumption for a wing with a high enough aspect ratio (length/chord). To verify, we calculate the maximum kinetic energy of each rotational mode for typical wing kinematics: flapping at 100 Hz with a stroke amplitude of 120° , and the angle of attack changing from 45° to 90° in one half of the half-stroke (i.e. one-quarter of a complete flapping cycle). This gives maximum angular velocities of $\dot{\phi} = 418 \text{ rad/sec}$ and $\dot{\psi} = 314 \text{ rad/sec}$. The moments of inertia about the wing base are $J_\phi = 45.3 \times 10^{-12} \text{ kg} \cdot \text{m}^2$ and $J_\psi = 1.7 \times 10^{-12} \text{ kg} \cdot \text{m}^2$. This gives maximum kinetic energies of

$$K_\phi = \frac{1}{2} J_\phi \dot{\phi}_{max}^2 = 3.96 \mu\text{J} \quad (7)$$

$$K_\psi = \frac{1}{2} J_\psi \dot{\psi}_{max}^2 = 0.084 \mu\text{J}. \quad (8)$$

Taking the ratio of these two terms gives

$$\frac{K_\phi}{K_\psi} \approx 47 \quad (9)$$

so we see that the vast majority of kinetic energy due to wing movement is stored in the flapping mode. Thus we can make the simplifying assumption that the inertial behavior of the wing is modeled by a beam with moment of inertia J_ϕ rotating about the ϕ axis (including inertia from the “added-mass” effect due to acceleration of the air, see [2]), and this behavior is linear.

2) *Aerodynamics*: The instantaneous aerodynamic force acting on the wing is typically broken into two components: lift and drag (F_L and F_D). We assume the aerodynamic energy terms are dominated by drag - i.e., the drag directly opposes motion of the actuator and thus dissipates energy; whereas we neglect the energy required to create a downward momentum jet of air during hover, and assume the lift force

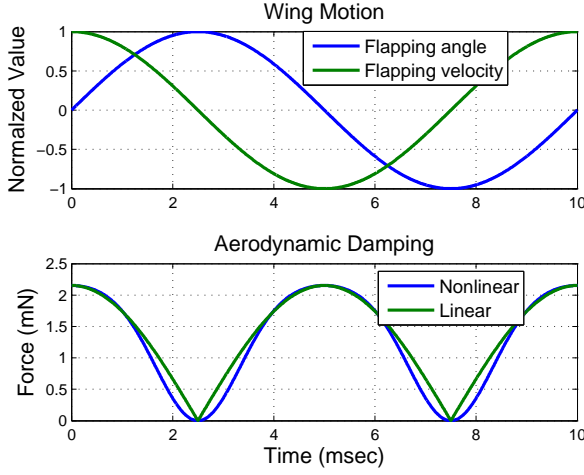


Fig. 13. Nonlinear and linearized aerodynamic drag forces over one flapping period for typical flapping kinematics, calculated using (10) and (11). Note that by convention, drag force is always defined to be positive.

does no work against gravity if the altitude of the vehicle does not change. The drag force is a function of flapping angular velocity $\dot{\phi}$,

$$F_D = \frac{1}{2} \rho \beta C_D(\alpha) \dot{\phi}^2 \quad (10)$$

where ρ is the ambient air density, $C_D(\alpha)$ is an angle-of-attack-dependent drag coefficient (determined experimentally in [7]) and β is a coefficient that depends on wing geometry (see [2] for details). The drag force acts at the wing center of pressure, a distance r_{cp} from the base of the wing. For a linear model, we desire a linear damper of the form $F_D = b\dot{\phi}$ where b is the damping coefficient. The drag force can be linearized about an operating point $[\dot{\phi}_0, \alpha_0]$, such that

$$F_D = \rho \beta C_D(\alpha_0) \dot{\phi}_0 \Delta \dot{\phi}. \quad (11)$$

Therefore b is given by

$$b = \rho \beta C_D(\alpha_0) \dot{\phi}_0. \quad (12)$$

Fig. 13 compares the nonlinear and linearized drag forces calculated using (10) and (11) over a full flapping cycle for typical flapping kinematics (flapping with 120° stroke amplitude at 100 Hz with an angle of attack of 45° and 90° at mid-stroke and the ends of the stroke respectively). We choose the point of maximum drag (which occurs at mid-stroke with $\alpha = 45^\circ$) for linearization, thus the linearized drag force always overestimates the actual drag force, giving a “worst case” estimate for aerodynamic behavior.

D. Complete model

Combining the linearized elements presented above yields the model pictured in Fig. 14, which is equivalent to that in Fig. 7. The equation of motion for this system is simply the classical result for a second-order spring-mass-damper,

$$m_{eq} \ddot{x} + b_{eq} \dot{x} + k_{eq} x = F \quad (13)$$

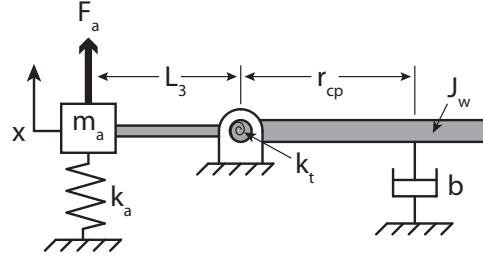


Fig. 14. A diagram of the linear dynamic model.

TABLE I
PHYSICAL PARAMETERS

Parameter	Symbol	Value	Units
Actuator mass	m_a	20	mg
Wing inertia	J_ϕ	45.3	mg·mm ²
Transmission ratio	T	2,857	rad/m
Radius to center of pressure	r_{cp}	10.1	mm
Aerodynamic damping	b	2.91	$\mu\text{N}\cdot\text{s/m}$
Actuator stiffness	k_a	300	N/m
Transmission stiffness	k_t	5,4872	$\mu\text{N}\cdot\text{m/rad}$
Equivalent mass	m_{eq}	390	mg
Equivalent damping	b_{eq}	0.2613	N·s/m
Equivalent spring constant	k_{eq}	344.8	N/m

where, mapping all relevant terms to the x coordinate,

$$m_{eq} = m_a + T^2 J_\phi \quad (14)$$

$$b_{eq} = T^2 r_{cp} b \quad (15)$$

$$k_{eq} = k_a + T^2 k_t. \quad (16)$$

Values for these parameters are given in Table I. The transfer function relating actuator displacement to force is then

$$\frac{X}{F} = \frac{1}{m_{eq}s^2 + b_{eq}s + k_{eq}} \quad (17)$$

and we compare the Bode plot for this transfer function to the identified model P_I in the following section. For convenience, we refer to the theoretical model as P_T .

IV. COMPARISON

The theoretical linear model P_T from (17) is compared to the identified model P_I in Fig. 15. We see reasonable agreement between the magnitude responses of P_T and P_I , with resonant frequencies of 133 Hz and 127 Hz respectively. This gives an error of approximately 5%, a significant improvement over the roughly 50% error in [1] (170Hz predicted vs. 110Hz actual). It is well known that while there is a one-to-one mapping of poles from a continuous time system to a discrete time system, the zeros obtained from discretely sampling a continuous-time system can be complicated functions of the sampling frequency [25], and this can affect the phase response. Thus, it is not cause for concern that the phase responses of the two systems do not match well. However, we note that the magnitude response of P_T depends heavily on the state $[\dot{\phi}_0, \alpha]$ used for linearization of the aerodynamic damping. The terms m_{eq} and k_{eq} are dependent on intrinsic geometric and material system properties, and are not explicitly dependent on linearization about

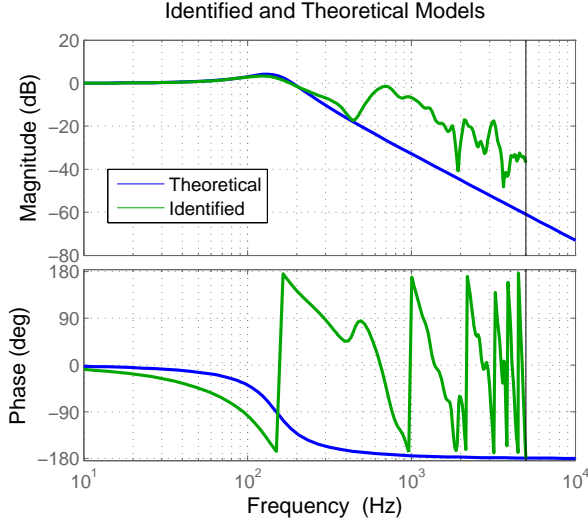


Fig. 15. Bode plots for the theoretical and identified models P_T and P_I are in reasonable agreement for magnitude, with resonant frequencies of 133 Hz and 127 Hz respectively.

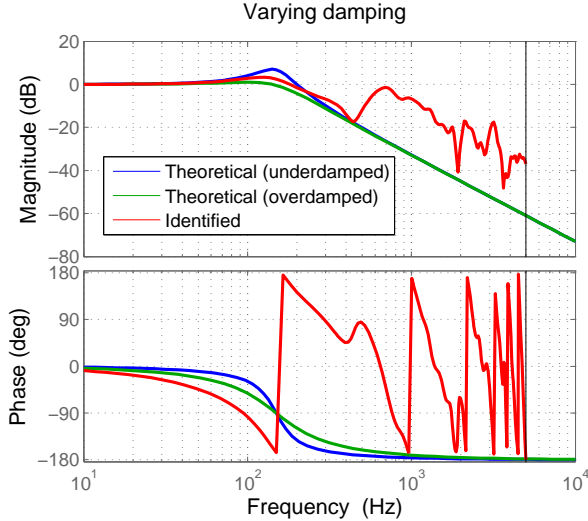


Fig. 16. Taking kinematic data from [2] allows selection of different states for linearization of the aerodynamic damping. Selecting an angle of attack $\alpha = 30^\circ$ results in an underdamped model, while $\alpha = 60^\circ$ gives an overdamped model. The good fit in Fig 15 resulted from $\alpha = 45^\circ$, and all three models use a flapping velocity of $\dot{\phi} = 392\text{rad/sec}$.

a state (unless the transmission ratio, T , is taken about a non-equilibrium position for the transmission, but we neglect this possibility). Choice of a different $[\phi_0, \alpha_0]$ for (11) can result in either over or under-damping of the theoretical model (Fig. 16).

V. IMPLICATIONS FOR VEHICLE DESIGN

The original design of the Harvard Microrobotic Fly [1] presented the undamped natural frequency of the system as

$$\omega_n = \sqrt{\frac{k_{eq}}{m_{eq}}} \quad (18)$$

and there it is correctly stated that wing flapping inertia should be minimized in order to maximize resonant frequency. However, transmission optimization was purely kinematic, i.e. T was maximized (based on limitations of the fabrication process which placed a lower bound on L_3) in order to maximize stroke amplitude for a given actuator displacement. Since a voltage-driven piezoelectric actuator acts as a force source, not a displacement source, this approach is not entirely realistic, as it does not take into account the effects of the transmission ratio on dynamic behavior. Here, we present the damped resonant frequency

$$\omega_d = \omega_n \sqrt{1 - \zeta^2} \quad (19)$$

in expanded form so the dependence on T can be seen:

$$\omega_d = \sqrt{\frac{m_a + T^2 J_\phi}{k_a + T^2 k_t}} \sqrt{1 - \frac{b_{eq}^2}{4(m_a + T^2 J_\phi)(k_a + T^2 k_t)}}. \quad (20)$$

This equation is plotted in Fig. 17 as a function of L_3 (remember that $T = 1/L_3$), and it is clear that, for the frequency range of interest, *resonant frequency increases with increasing L_3* (for very large L_3 , the system resonant frequency will asymptotically approach the resonant frequency of the unloaded actuator). Thus, the claim in [1] that transmission ratio should be maximized conflicts with the desire to increase resonant frequency. This result does not simply imply that transmission ratio should instead be minimized to maximize resonant frequency, as this would result in very small stroke amplitudes - e.g., a vehicle flapping at 1 kHz with only 5° of wing motion will likely generate negligible lift. Ultimately we seek to maximize the lift-to-weight ratio for a given vehicle, or maximize the lift force for a vehicle of fixed mass. For a linear model, as with the drag force, the lift force will be proportional to wing velocity. Thus we define a *characteristic wing velocity* as the product of resonant frequency and the stroke amplitude:

$$\dot{\phi}_{char} = |\phi| \omega_d \quad (21)$$

We use the DC stroke amplitude for this calculation, since, as discussed above, the magnitude at resonance is heavily dependent on the accuracy of the linearized damping term. The result, shown in Fig. 18, indicates that there is an optimal value for L_3 that gives maximum lift. Decreasing L_3 indefinitely will result in a decrease both resonant frequency and resulting lift force - an important result not considered in the original vehicle design.

Note that this analysis hinges on the assumption that the passive dynamics of wing rotation, which play a vital role in lift generation (see [2] for details), will remain sufficient to generate lift. In reality, these dynamics are also frequency-dependent, i.e. at very low frequencies, not enough aerodynamic force will be generated to cause the wing to rotate, so the angle of attack will remain near $\alpha = 90^\circ$ and little lift will be generated. Alternatively, at very high frequencies, high aerodynamic and inertial forces will cause the wing to “over-rotate” (i.e. α approaches 0°), and again, very little lift will be generated. Thus these results

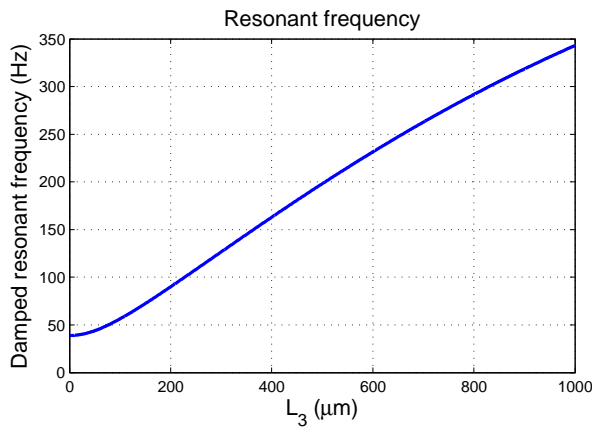


Fig. 17. Plot of (20), showing that resonant frequency increases with increasing L_3 for the linearized model P_T .

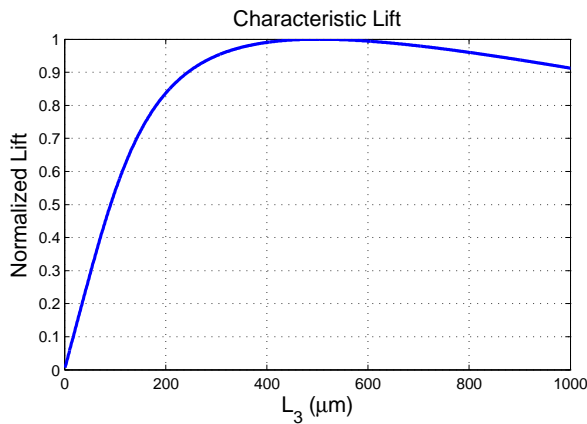


Fig. 18. Characteristic lift force as a function of L_3 for the linearized model P_T .

must be used with caution when extrapolated outside the neighborhood of flapping at 100 Hz.

VI. CONCLUSIONS

We have presented a linearized second order model that provides a reasonable fit to an identified model of a flapping-wing MAV. The linear model proves sufficient despite the inherently nonlinear nature of the system. The model provides insight into the design of the MAV system for flapping at resonance, especially when considering the transmission mechanism that maps actuator displacement to wing motion. The model will serve as a useful design tool for vehicle scaling, e.g., designing components for a vehicle with a larger mass, which will likely have larger wings and actuators and thus a lower resonant frequency. Designing FWMAVs to flap at resonance is an essential part of maximizing power efficiency for systems with limited payload and lift/weight ratio.

VII. ACKNOWLEDGEMENTS

This work was supported in part by the Army Research Laboratory (award number W911NF-08-2-0004), the Office of Naval Research (award number N00014-08-1-0919), and the Department of Defense (DoD) through the National

Defense Science and Engineering (NDSEG) graduate fellowship program (Ben Finio). The authors thank Pratheev Sreetharan for help with analysis of transmission linearity.

REFERENCES

- [1] R. Wood, "Design, fabrication, and analysis, of a 3DOF, 3cm flapping-wing mav," in *In Proc. IEEE/RSJ Int. Conf. on Intelligent Robots and Systems*, 2007, pp. 1576–1581.
- [2] J. Whitney and R. Wood, "Aeromechanics of passive rotation in flapping flight," *Journal of Fluid Mechanics*, vol. 1, no. 1, pp. 1–24, 2010.
- [3] R. Wood, E. Steltz, and R. Fearing, "Nonlinear performance limits for high energy density piezoelectric bending actuators," in *In Proc. IEEE Int. Conf. on Robotics and Automation*. IEEE, 2005, pp. 3633–3640.
- [4] R. Wood, "The first takeoff of a biologically inspired at-scale robotic insect," in *IEEE Trans. on Robotics*, vol. 24, 2008, pp. 341–347.
- [5] C. Ellington, "The aerodynamics of hovering insect flight. III. kinematics," *Philos. Trans. R. Soc. London Ser. B*, vol. 305, no. 1122, pp. 41–78, 1984.
- [6] —, "The aerodynamics of hovering insect flight. IV. aerodynamic mechanisms," *Philos. Trans. R. Soc. London Ser. B*, vol. 305, no. 1122, pp. 79–113, 1984.
- [7] M. Dickinson, F. Lehmann, and S. Sane, "Wing rotation and the aerodynamic basis of insect flight," *Science*, vol. 284, no. 5422, pp. 1954–1960, 1999.
- [8] J. Khatait, S. Mukherjee, and B. Seth, "Compliant design for flapping mechanism: A minimum torque approach," *Mechanism and Machine Theory*, vol. 41, no. 1, pp. 3–16, 2006.
- [9] T. Tantanawat and S. Kota, "Design of compliant mechanisms for minimizing input power in dynamic applications," *Journal of Mechanical Design*, vol. 129, p. 1064, 2007.
- [10] R. Madangopal, G. Student, Z. Khan, and S. Agrawal, "Biologically Inspired Design Of Small Flapping Wing Air Vehicles Using Four-Bar Mechanisms And Quasi-steady Aerodynamics," *Journal of Mechanical Design*, vol. 127, p. 809, 2005.
- [11] R. Madangopal, Z. Khan, and S. Agrawal, "Energetics-based design of small flapping-wing micro air vehicles," *IEEE/ASME Trans. on Mechatronics*, vol. 11, no. 4, pp. 433–438, 2006.
- [12] S. Baek, K. Ma, and R. Fearing, "Efficient resonant drive of flapping-wing robots," in *In Proc. IEEE/RSJ Int. Conf. on Intelligent Robots and Systems*. IEEE, 2009, pp. 2854–2860.
- [13] Z. Khan and S. Agrawal, "Design and optimization of a biologically inspired flapping mechanism for flapping wing micro air vehicles," in *In Proc. IEEE Int. Conf. on Robotics and Automation*. IEEE, 2007, pp. 373–378.
- [14] G. Gremillion and J. Humbert, "System identification of a quadrotor micro air vehicle," in *AIAA Conf. on Atmospheric Flight Mechanics*, 2010.
- [15] R. Wood, K. Cho, and K. Hoffman, "A novel multi-axis force sensor for microrobotics applications," *Smart Materials and Structures*, vol. 18, p. 125002, 2009.
- [16] Pérez-Arancibia, Néstor O. and Whitney, John P. and Wood, Robert J., "Lift force control of a flapping-wing microrobot," in *American Controls Conf.*, 2011.
- [17] M. Sitti, D. Campolo, J. Yan, and R. Fearing, "Development of PZT and PZN-PT based unimorph actuators for micromechanical flapping mechanisms," in *In Proc. IEEE Int. Conf. on Robotics and Automation*, vol. 4. IEEE, 2005, pp. 3839–3846.
- [18] D. Campolo, R. Sahai, and R. Fearing, "Development of piezoelectric bending actuators with embedded piezoelectric sensors for micromechanical flapping mechanisms," in *In Proc. IEEE Int. Conf. on Robotics and Automation*, vol. 3, 2003, pp. 3339–3346.
- [19] R. Wood, E. Steltz, and R. Fearing, "Optimal energy density piezoelectric bending actuators," *Sensors and Actuators A: Physical*, vol. A 119, pp. 476–488, 2005.
- [20] E. Steltz and R. Fearing, "Dynamometer power output measurements of miniature piezoelectric actuators," *IEEE/ASME Trans. on Mechatronics*, vol. 14, no. 1, pp. 1–10, 2009.
- [21] L. Marks, *Marks' Standard Handbook for Mechanical Engineers*, E. Avallone, T. Baumeister III, and A. Sadegh, Eds. McGraw Hill, 2007.
- [22] E. Steltz and R. Fearing, "Dynamometer power output measurements of piezoelectric actuators," in *In Proc. IEEE/RSJ Int. Conf. on Intelligent Robots and Systems*. IEEE, 2007, pp. 3980–3986.

- [23] R. Wood, S. Avadhanula, R. Sahai, E. Steltz, and R. Fearing, "Micro-robot Design Using Fiber Reinforced Composites," *J. Mech. Design*, vol. 130, pp. 52 304–52 315, 2008.
- [24] E. Steltz, M. Seeman, S. Avadhanula, and R. Fearing, "Power electronics design choice for piezoelectric microrobots," in *In Proc. IEEE/RSJ Int. Conf. on Intelligent Robots and Systems*, 2006, pp. 1322–1328.
- [25] K. Åström, P. Hagander, and J. Sternby, "Zeros of sampled systems," *Automatica*, vol. 20, no. 1, pp. 31–38, 1984.